Available online at www.sciencedirect.com
ScienceDirect
Acta Materialia 59 (2011) 4886–4894
Acta MATERIALIA
www.elsevier.com/locate/actamat

Thermoelastic properties of ScB_2, TiB_2, YB_4 and HoB_4: Experimental and theoretical studies

A. Waśkowska [a], L. Gerward [b,*], J. Staun Olsen [c], K. Ramesh Babu [d], G. Vaitheeswaran [d], V. Kanchana [e], A. Svane [f], V.B. Filipov [g], G. Levchenko [g], A. Lyaschenko [g]

[a] Institute of Low Temperature and Structure Research, Polish Academy of Sciences, Wroclaw, Poland
[b] Department of Physics, Technical University of Denmark, Lyngby, Denmark
[c] Niels Bohr Institute, Oersted Laboratory, University of Copenhagen, Copenhagen, Denmark
[d] ACRHEM, University of Hyderabad, Prof. C. R. Rao Road, Gachibowli, Hyderabad 500 046, Andhra Pradesh, India
[e] Department of Physics, IIT Hyderabad, Ordnance Factory Estate, Yeddumailaram 502 205, Andhra Pradesh, India
[f] Department of Physics and Astronomy, Aarhus University, Aarhus, Denmark
[g] Institute for Problems of Materials Science, Academy of Sciences of Ukraine, Kiev, Ukraine

Received 2 March 2011; received in revised form 14 April 2011; accepted 14 April 2011
Available online 9 May 2011

Abstract

High-pressure X-ray diffraction in ScB_2, TiB_2, YB_4 and HoB_4 powders and single crystals has been studied using synchrotron radiation as well as conventional X-rays. The experimental results are supported by calculations using density functional theory. ScB_2, YB_4 and HoB_4 are hard materials (bulk modulus 180–200 GPa), while TiB_2 may be classified as superhard (bulk modulus about 260 GPa). We report here first experimental and theoretical determinations of the bulk modulus for HoB_4 (195(5) and 198.2 GPa, respectively), and first experimental values of the bulk modulus for ScB_2 (196(2) GPa) and YB_4 (185(4) GPa). No pressure-induced phase transformations are observed in any of the above borides up to about 20 GPa. A continuous temperature-driven orthorhombic distortion is observed for HoB_4 below 285 K. Values of the thermal expansion coefficient are reported for ScB_2 and HoB_4 at 293, 200 and 100 K. The thermoelastic behavior is explained in terms of bonding characteristics.

Keywords: Borides; Bulk modulus; Elastic constants; Thermal expansion; Density functional theory

1. Introduction

Metal borides are hard and heat resistant, making them important for many high-technology applications [1–4]. The discovery of superconductivity in MgB_2 with a critical temperature $T_c = 39$ K [5] has further stimulated theoretical and experimental studies on diborides [6,7]. Transition-metal diborides, such as TiB_2, CrB_2 and ZrB_2, are commonly employed in high-temperature service applications. Knowledge of thermoelastic properties of metal borides is therefore essential. Extensive studies have been carried out on mechanical parameters, such as the elastic constants, bulk modulus, compressibility and shear modulus, for a number of hexagonal AlB_2-type compounds. Primarily, these studies have been first-principles calculations [8–13], but recently experimental studies have also been reported [14–16].

Heavy rare-earth tetraborides have interesting multistep phase transitions at low temperatures, involving commensurate and incommensurate magnetic structures originating from competitions between various interactions and the geometrically frustrated lattice of the rare-earth ions [17–23]. In particular, tetragonal HoB_4, with its $4f^{10}$ electron configuration of Ho^{3+}, orders antiferromagnetically at the Néel temperature $T_{N1} = 7.1$ K, followed by a another first-order transition at a second Néel

* Corresponding author.
E-mail address: gerward@fysik.dtu.dk (L. Gerward).

1359-6454/$36.00 © 2011 Acta Materialia Inc. Published by Elsevier Ltd. All rights reserved.
doi:10.1016/j.actamat.2011.04.030

temperature $T_{N2} = 5.6$ K. Neutron diffraction studies have shown that the critical behavior of HoB_4 is accompanied by complex diffuse scattering from broad fluctuating regions of coexisting phases I and II with short- and long-range order [24,25]. The magnetic susceptibility, measured parallel and perpendicular to the tetragonal c-axis, has a remarkable anisotropy [26], indicating different ordering mechanisms along the c-axis and in the (a, b)-plane. For example, only the transition at T_{N2} is present when the applied magnetic field is perpendicular to the c-axis.

In the present work we have grown single crystals of ScB_2, TiB_2, YB_4 and HoB_4 and determined the bulk modulus, thermal expansion and other thermoelastic properties of these compounds. Most of the experimental work was performed using synchrotron radiation, but conventional X-rays were applied for a crystal-structure determination of HoB_4. The experimental results are supported by extensive calculations using density functional theory. Preliminary results for HoB_4 were presented at the 48th European High-Pressure Research Group International Conference, 25–29 July 2010, in Uppsala, Sweden [27].

2. Experimental

2.1. Crystal growth

Single crystals of ScB_2, TiB_2, YB_4 and HoB_4 were prepared in a multistage process: (1) synthesis of powders; (2) compacting into rods and sintering; and (3) growth of single crystals. At each stage the single-phase product was confirmed by X-ray diffraction and other methods. Here we will consider in detail the first and third stages.

TiB_2 was synthesized from the metallic elements titanium and boron, which were mixed and then melted by an electric arc. The product was powdered after cooling. ScB_2, YB_4 and HoB_4 were produced by reduction of the corresponding metal oxides in the presence of boron according to the following chemical reactions:

$$Sc_2O_3 + 7B \rightarrow 2ScB_2 + 3BO\uparrow \quad (1)$$

$$Me_2O_3 + 11B \rightarrow 2MeB_4 + 3BO\uparrow \quad (Me = Y, Ho) \quad (2)$$

The reactions proceeded at high temperature (1900 K) in vacuum. The normality was 4 N of the initial Sc_2O_3 and Ho_2O_3, and 5 N of Y_2O_3. The purity of the initial amorphous boron was better than 99.5 wt.%. Volatile impurities in boron were eliminated during the synthesis and zone melting because of the high temperature.

The powders were cold-molded into rods of 8 mm diameter and 60 mm length and sintered at 2000 K in vacuum. Single crystals were grown by crucible-free inductive floating-zone melting in argon atmosphere (pressure less than 2.5 MPa). The above method is particularly suitable for purification and growth of large perfect single crystals of refractory borides, considering their metal-like conductivity, high melting point and high reactivity in the molten state. The crystallization rate, speed of rotation, gas pressure, number of zone passages, etc. were optimized for each boride. In particular, ScB_2 single crystals were grown by the so-called zone-leveling technique [28]. The purity was better than 99.999 mass% for ScB_2, YB_4 and HoB_4, and 99.99 mass% for TiB_2. The single crystals were 4–6 mm in diameter and about 50 mm in length. X-ray Laue photographs illustrate the high quality of the crystals (Fig. 1). ScB_2 and HoB_4 crystals from the same batches have been studied by the de Haas–van Alphen effect [29,30], and YB_4 samples by nuclear magnetic resonance [31], thereby confirming the crystal perfection. The composition range of homogeneity is narrow for ScB_2, YB_4, HoB_4, but somewhat wider for TiB_2 [32].

2.2. X-ray diffraction

Room temperature, high-pressure powder X-ray diffraction spectra were recorded using synchrotron white radiation and the energy-dispersive method. High-pressures were obtained in a Syassen–Holzapfel-type diamond-anvil cell. Powdered samples were placed in a hole with a diameter of 200 μm in an Inconel gasket, pre-indented to a thickness of 60 μm. A 16:3:1 methanol:ethanol:water mixture was used as the pressure-transmitting medium. The pressure was determined from the equation of state of NaCl [33] for HoB_4, and by the ruby luminescence method [34] for the other samples. At each pressure, values for the lattice parameters and the unit cell volume were derived from the diffraction spectrum and refined using the PURUM code [35]. Compression curves through the experimental pressure–volume data points were described by the Birch–Murnaghan equation of state [36]:

$$P = \frac{3}{2}B_0\left(x^{-7/3} - x^{-5/3}\right)\left[1 - \frac{3}{4}(4 - B_0')\left(x^{-2/3} - 1\right)\right] \quad (3)$$

where $x = V/V_0$, and V and V_0 are the unit cell volumes at pressure P and zero pressure, respectively. The zero-pressure bulk modulus B_0 and its pressure derivative B_0' are fitting parameters. Usually there is some correlation between the values of B_0 and B_0'. We therefore constrained B_0' to the typical value 4.00 in order to facilitate comparisons of B_0 values for the various borides.

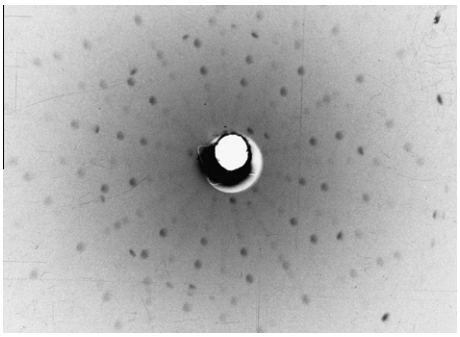

Fig. 1. X-ray Laue pattern of HoB_4 single crystal. The growth direction is close to [0 0 1].

The evolution of the unit cell parameters with temperature was studied by single-crystal diffraction, using monochromatized synchrotron radiation and a four-circle Huber diffraction unit equipped with a point detector. The wavelength was adjusted to 0.7000(1) Å. The temperature of the samples was lowered in small steps down to 100 K, using an Oxford Cryojet based on liquid nitrogen. Unit cell parameters at each temperature were calculated by least-squares refinement using the setting angles of 24 high-angle Bragg reflections. Diffraction data for a single-crystal-structure determination of HoB_4 were collected at room temperature using conventional X-rays (Mo Kα) and an Oxford diffraction unit equipped with a CCD detector. The refinement converged with conventional discrepancy factors $R_1 = 0.023$ and $wR = 0.054$ for 320 reflections with $F_0 > 4\sigma(F_0)$. A rocking ω-scan showed that the mosaicity of the samples was about 0.16°, again demonstrating the high quality of the crystals.

3. Computational procedures

ScB_2 and TiB_2 are hexagonal, with an AlB_2-type structure and space group *P6/mmm* (#191). The metal atom is situated at the 1*a* site (0, 0, 0) and the boron atoms at 2*d* (1/3, 2/3, 0.5) [28]. YB_4 and HoB_4 are tetragonal, with a ThB_4-type structure and space group *P4/mbm* (#127) [37]. The metal atom is situated at 4*g* (x, $x + 1/2$, 0); the boron atoms B1 at 4*e* (0, 0, z), B2 at 4*h* (x, y, 0.5) and B3 at 8*j* (x, y, 0.5).

3.1. ScB_2, TiB_2 and YB_4

First-principles electronic structure calculations were performed using the Cambridge Series of Total Energy Package based on density functional theory [38]. The electron–ion interactions were described by Vanderbilt-type ultrasoft pseudo-potentials [39], and the electron–electron interactions by an exchange correlation potential in the generalized gradient approximation according to the Perdew, Burke and Ernzerhof scheme [40]. To confirm the convergence of the calculations for the Brillouin-zone sampling, we tested the dependence of the total energy on the plane wave cut-off energy and on the *k*-point mesh according to the grid scheme of Monkhorst and Pack [41]. It was found that the total energy is minimum up to three decimals for the cut-off energy of 380 eV and the *k*-point set 10 × 10 × 8 for TiB_2 and ScB_2. The corresponding data for YB_4 are 420 eV and 10 × 10 × 12. Therefore, we chose the above data for the calculations. The self-consistent convergence of the total energy is 5×10^{-7} eV atom^{-1} and the maximum force on the atom is 10^{-4} eV Å^{-1}.

3.2. HoB_4

The heavy rare-earth tetraboride HoB_4 is a strongly correlated *f*-electron system, which needs special theoretical treatment. The electronic structure of HoB_4 was calculated by the linear muffin-tin orbital method [42] in the full-potential implementation of Methfessel et al. [43]. In this method, the crystal volume is divided into touching atomic muffin-tin spheres and the remaining interstitial volume. The electron wave functions have been expanded in terms of numerical solutions to the crystal Hamiltonian within the spheres, joined smoothly to decaying tails of Hankel-type in the interstitial volumes. Two different decay rates were used, and the expansion inside the spheres were cut off at $L_{max} = 5$. Muffin-tin orbitals of the principal character Ho(6*s*, 5*p*, 5*d*, 4*f*) and B(2*s*, 2*p*) were included. All scalar-relativistic effects were included. The charge density sampling was performed using a 6 × 6 × 6 Monkhorst–Pack mesh of *k*-points. Following Yin and Pickett [23], ferromagnetic alignment of the Ho spin magnetic moments was assumed. The calculations were carried out using the local spin density approximation (LSDA) as well as LSDA with local Coulomb correlation (LSDA + *U*) for exchange and correlation effects. For the screened *f*–*f* Coulomb parameter, the value of $U = 8$ eV was used [23] with double counting correction, as given by the fully localized limit [44].

Experimental values of the *c*/*a* ratio of the tetragonal unit cell and of the internal atomic coordinates at ambient conditions were used throughout, i.e. no theoretical optimization of these parameters was attempted. Our experiments have shown that the *c*/*a* ratio is about 0.565 at ambient conditions and decreases slowly with increasing pressure. However, the variation is less than 1% within the observed pressure range and therefore considered negligible in the calculations.

4. Results and discussions

4.1. ScB_2 and TiB_2

The evolution of the unit cell parameters of ScB_2 with decreasing temperature is shown in Fig. 2a. It is seen that the cell dimensions are nearly constant in the (*a, b*)-plane, while a slight temperature dependence is evident for the *c*-axis. This is consistent with the nature of bonding in the structure, which is built up of parallel layers of six-member boron rings in the (*a, b*)-plane alternating with hexagonal layers of Sc ions [28]. Strong covalent B–B bonds ensure stability and stiffness within the (*a, b*)-plane, whereas bonding along the *c*-direction involves the weaker Sc–Sc and Sc–B interactions. The average linear thermal expansion coefficient along the *c*-direction was determined as $\alpha_c = 2.8 \times 10^{-6}$ K^{-1}. Values of the volume expansion coefficient α_V at selected temperatures (Table 1) have been derived from a polynomial fit to the experimental temperature–volume data points.

The *c*/*a* ratio decreases with decreasing temperature, as seen in Fig. 2b. The scatter of the data points may be due to the relaxation of microstrains accumulated in the structure during cooling. The room temperature *c*/*a* ratio of ScB_2 is 1.117, which is larger than the 1.065 observed

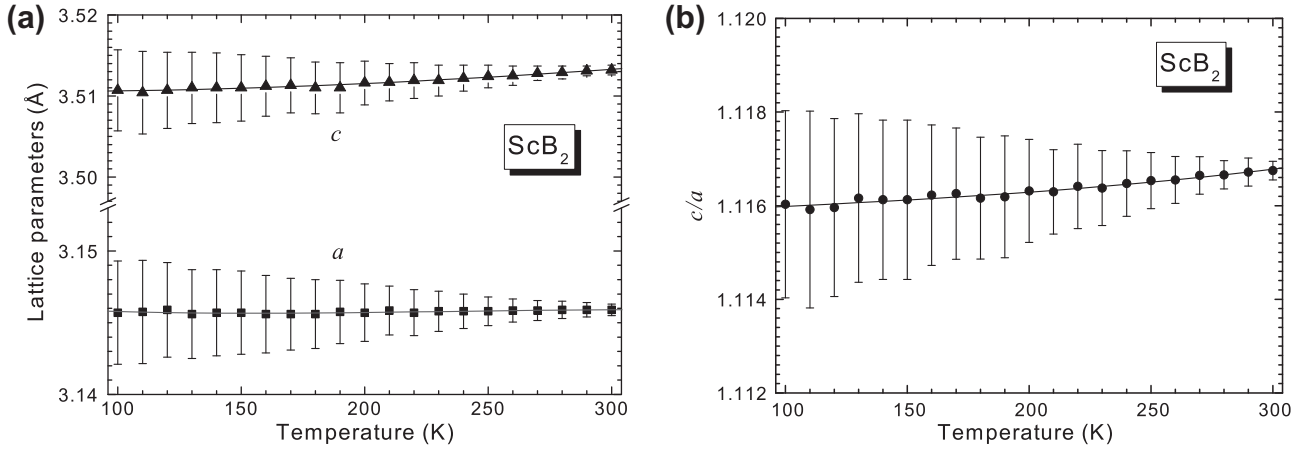

Fig. 2. Evolution of the unit cell parameters of ScB_2 with decreasing temperature. (a) Lattice parameters a and c. (b) The c/a ratio.

Table 1
Experimental values of the volume thermal expansion coefficient α_V for ScB_2 and HoB_4 in units of 10^{-6} K^{-1}.

Temperature (K)	ScB_2	HoB_4
293	15.70	7.94
200	9.13	6.21
100	2.06	4.35

The relative uncertainty is about 5%.

for TiB_2. As shown below, this difference explains why TiB_2 is considerably less compressible (*i.e.* has a larger bulk modulus) than ScB_2.

Figs. 3 and 4 show the compression curves of ScB_2 and TiB_2, respectively. From a least-squares fit of Eq. (3) to the experimental pressure–volume data, we obtain $B_0 = 196.4 \pm 2.0$ GPa for ScB_2 and $B_0 = 260.0 \pm 3.0$ GPa for TiB_2. To the best of our knowledge, we report here the first experimental determination of the bulk modulus for ScB_2. A comparison with other experimental and theoretical data is given in Table 2. It is seen that data for ScB_2 are scarce. In contrast, there are numerous high-pressure studies on TiB_2.

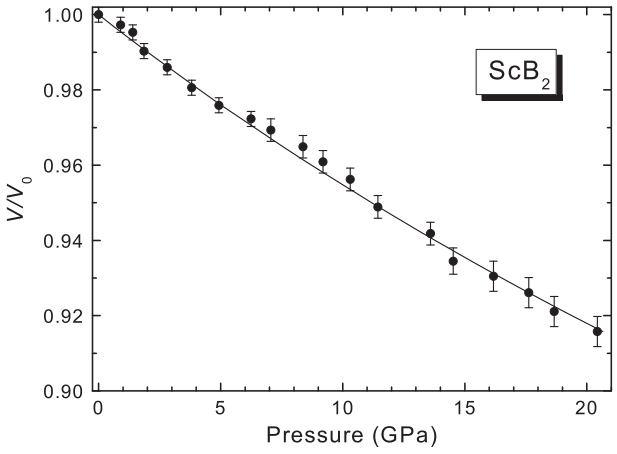

Fig. 3. Compression curve of ScB_2. The solid line is the fit of the Birch–Murnaghan Eq. (3) to the experimental pressure–volume data points.

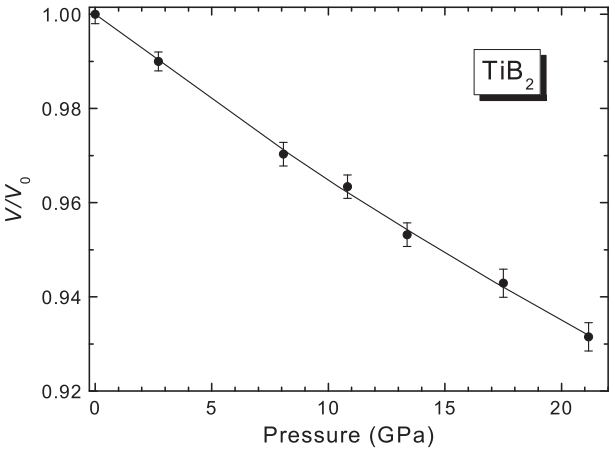

Fig. 4. Compression curve of TiB_2. The solid line is the fit of the Birch–Murnaghan Eq. (3) to the experimental pressure–volume data points.

Calculated values of the elastic constants C_{ij}, longitudinal wave velocity v_l, transverse wave velocity v_t, average sound velocity v_m, Debye temperature Θ_D and anisotropy factor A of ScB_2 and TiB_2 are shown in Table 3, together with literature data for comparison. Table 4 lists calculated values of some elastic parameters for polycrystalline ScB_2 and TiB_2 in the Voigt–Reuss–Hill (VRH) approximation: bulk moduli B_V, B_R, B_{VRH}, shear moduli G_V, G_R, G_{VRH}, Lamé constant λ_V, λ_R, λ_{VRH}, compressibility β_{VRH}, Young's modulus Y, Poisson's ratio v and the ratio B_{VRH}/G_{VRH}.

A material is considered hard if it has a high bulk modulus, a high shear strain modulus and a small structural anisotropy. Given the parameters in Tables 3 and 4, it is evident that TiB_2 is considerably harder than the isostructural ScB_2. This can be explained by the nature and strength of the bonding. It has been shown that bonding is a combination of ionic, covalent and metallic interactions in 3*d* transition metal (TM)-diborides [3,10]. The covalent nature of the B–B bonds is common to all TM-diborides and does not change significantly within the series. However, the covalent nature of the TM–B bond increases with increasing occupation of the *d*-orbital. Thus,

Table 2
Calculated and experimental values of the lattice parameters a and c, unit cell volume V and bulk modulus B_0 for ScB_2, TiB_2 YB_4 and HoB_4.

Compound	Theory	Experiment	Refs.
ScB_2			
a, c (Å)	3.138, 3.525	3.1459(9), 3.5131(7)	Present work
		3.1482(1), 3.5148(1)	Levchenko et al. [28]
B_0 (GPa)	187.1	196(2)	Present work
	198.9		Shein and Ivanovskii [11]
TiB_2			
a, c (Å)	3.0292, 3.2198	3.032(2), 3.229(4)	Present work
		3.0292(3), 3.2284(3)	Moehr et al. [45]
B_0 (GPa)	250.0	260(3)	Present work
	255–260		Wang et al. [12]
	263.2		Shein and Ivanovskii [11]
	245		Peng et al. [46]
	249–304		Panda and Chandran [47]
	292		Pereira et al. [48]
		236(23)	Amulele et al. [49]
		240	Munro [4]
YB_4			
a, c (Å)	7.087, 4.011	7.106(4), 4.020(4)	Present work
		7.111(3), 4.017(2)	Guette et al. [52]
B_0 (GPa)	180.7	185(4)	Present work
	178.1		Herzig [53]
HoB_4			
a, c (Å)		7.082(2), 4.004(1)	Present work (synchr. rad.)
		7.084(2), 4.006(3)	Present work (X-ray tube)
		7.085, 4.004	Etourneau et al. [17]
V_0 (Å^3)	204.8	200.9(1)	Present work (LSDA + U theory)
	197.4		Present work (LSDA theory)
B_0 (GPa)	198.2	195(5)	Present work (LSDA + U theory)
	188.4		Present work (LSDA theory)

Uncertainties, stated within parentheses, are in units of the last decimal place.

Table 3
Elastic constants C_{ij}, longitudinal wave velocity v_l, transverse wave velocity v_t, average sound velocity v_m, Debye temperature Θ_D and anisotropy factor A of ScB_2 and TiB_2.

Property	ScB_2	TiB_2
C_{11} (GPa)	497.6 (508.5)[a]	660.4 (670.9)[a] (660)[b] (588–711)[c]
C_{12} (GPa)	40.80 (41.9)[a]	67.06 (64.0)[a] (48)[b] (17–410)[c]
C_{13} (GPa)	66.49 (73.5)[a]	98.73 (100.9)[a] (93)[b] (84–320)[c]
C_{33} (GPa)	370.2 (373.3)[a]	462.5 (472.9)[a] (432)[b] (224–440)[c]
C_{44} (GPa)	181.3 (189.5)[a]	259.5 (266.6)[a] (260)[b] (232–250)[c]
v_l (km s^{-1})	11.07	11.55 (11.65)
v_t (km s^{-1})	7.308	7.615 (7.470) [d]
v_m (km s^{-1})	7.336	7.642
Θ_D (K)	993.9 (1020) [e]	1092.9 (1190)[d]
A	0.74 (0.73)[a]	0.70 (0.71)[a] (0.821)[d]

Values in parentheses are literature data for comparison.
[a] Shein and Ivanovskii [11].
[b] Spoor et al. [50].
[c] Perottoni et al. [8] (expt.).
[d] Dodd et al. [51].
[e] Levchenko et al. [28].

Table 4
Calculated values of some elastic parameters for polycrystalline materials of ScB_2 and TiB_2 in the Voigt, Reuss and Voigt–Reuss–Hill approximation: bulk modulus (B_V, B_R, B_{VRH}), shear modulus (G_V, G_R, G_{VRH}), the ratio B_{VRH}/G_{VRH}, the Lamé constant (λ_V, λ_R, λ_{VRH}), compressibility (β_{VRH}), Young's modulus (Y) and Poisson's ratio (v).

Property	ScB_2	TiB_2
B_V (GPa)	189.3	254.7
B_R (GPa)	187.1	250.0
B_{VRH} (GPa)	188.2 (198.9)[a]	252.3 (263.2)[a] (276)[b]
G_V (GPa)	197.3	263.7
G_R (GPa)	193.6	258.3
G_{VRH} (GPa)	195.5 (201.4)[a]	261.0 (268.9)[a] (252)[b]
B_{VRH}/G_{VRH}	0.96	0.97
λ_R (GPa)	57.98	77.80
λ_{VRH} (GPa)	57.86 (64.6)[a]	78.33 (83.9)[a]
Y (GPa)	435.6 (452)[a]	582.2 (601.9)[a] (579)[b]
v	0.114 (0.121)[a]	0.115 (0.119)[a] (0.15)[b]
β_{VRH} (10^{-3} GPa^{-1})	5.31 (5.03)[a]	3.96 (3.80)[a] (3.62)[b]

[a] Shein and Ivanovskii [11].
[b] Dodd et al. [51].

hybridization between boron p-orbitals and TM d-states increases with decreasing ionic radius of the 3d metal. The Sc–B bonds are weaker than the Ti–B bonds, since the ionic radius of Sc is larger than that of Ti ($R_{Sc3+} = 0.745$ Å and $R_{Ti3+} = 0.67$ Å). The same is true for the TM–TM bonds. It follows that ScB_2 has a larger structural anisotropy and consequently a higher compressibility (*i.e.* a smaller bulk modulus) than TiB_2.

4.2. YB_4

The lattice parameters of tetragonal YB_4 at ambient conditions, as determined in the diamond-anvil cell, are $a = 7.106(4)$ Å and $c = 4.020(4)$ Å. These values are in good agreement with literature data [52] (Table 2). Experimental and calculated atomic positions in the unit cell are given in Table 5. Fig. 5 shows the compression curve of YB_4. From a least-squares fit of Eq. (3) to the experimental pressure–volume data we obtain $B_0 = 185.4 \pm 3.5$ GPa (Table 2). To the best of our knowledge, this is the first experimental value of the bulk modulus reported for YB_4. Our experimental value compares well with the 180.7 GPa calculated in the present work, and with the 178.1 GPa calculated by P. Herzig (private communication). See also Ref. [53].

4.3. HoB_4

Fig. 6a shows the tetragonal HoB_4 structure projected on the (*a, b*)-plane. The self-bonding of boron results in a rigid network, consisting of B_6 octahedra (B1 and B2 atoms) and three-coordinated boron (B3). The octahedra are linked along the *c*-direction through B1–B1 bonds. The main results of the single-crystal structure refinement based on X-ray diffraction data are given in Tables 6 and 7. It follows that the Ho−Ho distances, corresponding to the magnetic dipolar interactions J_1 and J_2 in the Shastry–Sutherland lattice [54] (Fig. 6b), are 3.646(1) and 3.671(1) Å, respectively. The geometric frustration of the

Table 5
Experimental and calculated atomic positions in tetragonal YB_4 (space group *P4/mbm*).

Atom	Site symmetry	Atomic position expt. [52]	Atomic position calc. (present work)
Y	4*g* (*x*, 1/2 + *x*, 0)	$x = 0.3179$	$x = 0.3179$
B1	4*e* (0, 0, *z*)	$z = 0.2027$	$z = 0.2028$
B2	4*h* (*x*, 1/2 + *x*, 1/2)	$x = 0.0871$	$x = 0.0871$
B3	8*j* (*x*, *y*, 1/2)	$x = 0.1757$	$x = 0.1760$
		$y = 0.0389$	$y = 0.0387$

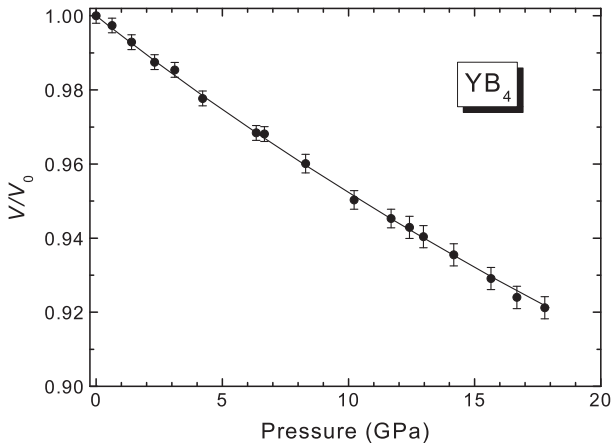

Fig. 5. Compression curve of YB_4. The solid curve is the fit of the Birch–Murnaghan Eq. (3) to the experimental pressure–volume data points.

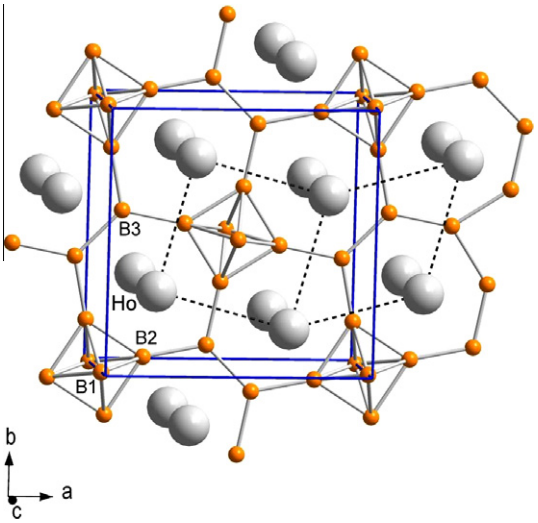

Fig. 6. (a) Tetragonal HoB_4 structure projected on the (*a, b*)-plane. The broken lines represent the HoB_6 and HoB_2 units. See Table 6 for definitions of B1–B3. (For interpretation of the references to colours in this figure, the reader is referred to the web version of this paper.)

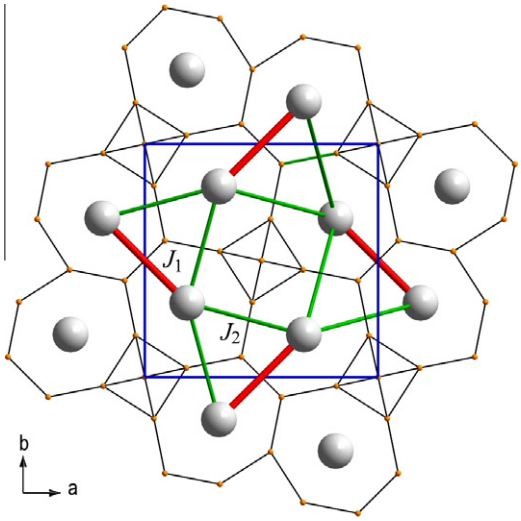

Fig. 6. (b) Two-dimensional sublattice of Ho^{3+}-ions in the Shastry–Sutherland lattice with the orthogonal arrangement of nearest-neighbour Ho-dipoles (shown by thick lines). See the text for definitions of J_1 and J_2. (For interpretation of the references to colours in this figure, the reader is referred to the web version of this paper.)

Table 6
Atomic positions in tetragonal HoB4 (space group *P4/mbm*); $a = 7.0842(16)$ Å and $c = 4.006(3)$ Å.

Atom	Site symmetry	Atomic position	$U_{11} = U_{22}$	U_{33}
Ho	4*g* (*x*, 1/2 + *x*, 0)	$x = 0.31803$ (3)	4.6 (0.1)	8.9 (0.2)
B1	4*e* (0, 0, *z*)	$z = 0.2062$ (21)	9.2 (1.9)	9.9 (2.9)
B2	4*h* (*x*, 1/2 + *x*, 1/2)	$x = 0.0859$ (8)	4.4 (1.7)	9.2 (2.3)
B3	8*j* (*x*, *y*, 1/2)	$x = 0.1773$ (7)	$U_{11} = 5.4$ (1.9)	7.1 (1.7)
		$y = 0.0391$ (7)	$U_{22} = 4.1$ (1.8)	

Anisotropic thermal displacements $U_{ii} \times 10^3$ are given in Å^2.

Table 7
Main interatomic distances in tetragonal HoB_4.

Atoms	Distance (Å)	Atoms	Distance (Å)
Ho–$Ho1_{-x,2-y,z}$	3.646 (1)	B1–$B1_{-x,-y,-z}$	1.652 (17)
Ho–$Ho1_{-y,x,z}$	3.671 (1)	B1–B3	1.743 (7)
Ho–B1	2.724 (3)	B2–B3	1.710 (6)
Ho–B3	2.731 (3)	B3–B3	1.819 (7)

Ho^{3+} sublattice leads to macroscopic strains, resulting in unit cell distortions at low temperatures, as discussed below.

An earlier report on the thermal expansion in the temperature range 317–1297 K, based on a quartz optical dilatometer method, did not show any characteristic features [55]. The evolution of the single-crystal unit cell measured in the present study is shown in Fig. 7. A distortion appears in the (*a, b*)-plane below a critical temperature $T_c \approx 285$ K. The variations of *a* and *b* are nearly symmetrical, but without saturation. The variation in the *c*-axis is monotonous. The volume as a function of temperature shows a normal behavior. Values of the thermal expansion coefficient α_V at selected temperatures are given in Table 1. Our room temperature value $7.94 \times 10^{-6}\,K^{-1}$ is in good agreement with $7.85 \times 10^{-6}\,K^{-1}$ reported by Severyanina et al. [55]. The unit cell angles remain rectangular over the whole temperature range observed. The continuously growing distortion, lowering the symmetry to orthorhombic, can be interpreted as a Landau-type phase transition [56].

Following symmetry rules, the lattice distortion is described by the spontaneous strain ε_s, the components of which are given by

$$e_1 = (a - a_0)/a_0 \quad (4.a)$$

$$e_2 = (b - a_0)/a_0 \quad (4.b)$$

$$e_3 = (c - c_0)/c_0 \quad (4.c)$$

where a_0 and c_0 are the tetragonal lattice parameters, and *a*, *b* and *c* describe the orthorhombic unit cell. Referring to Figs. 8 and 9, the symmetry breaking strain in HoB_4 is

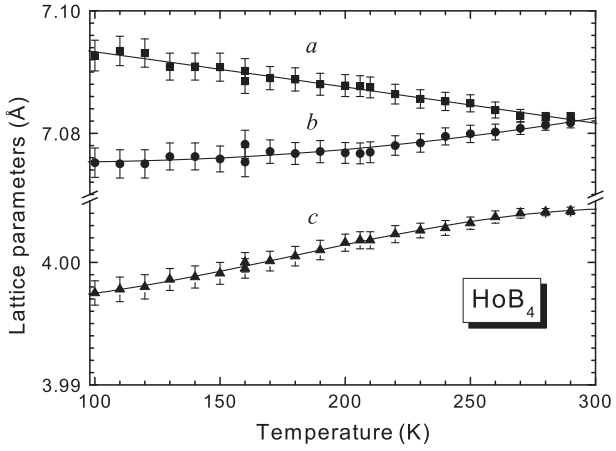

Fig. 7. Evolution of the unit cell parameters *a*–*c* of HoB_4 with decreasing temperature.

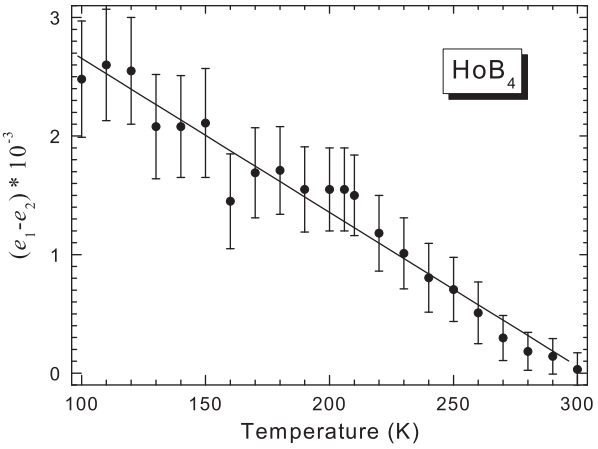

Fig. 8. Spontaneous strain, e_1–e_2, as a function of temperature, indicating a symmetry change at about 285 K.

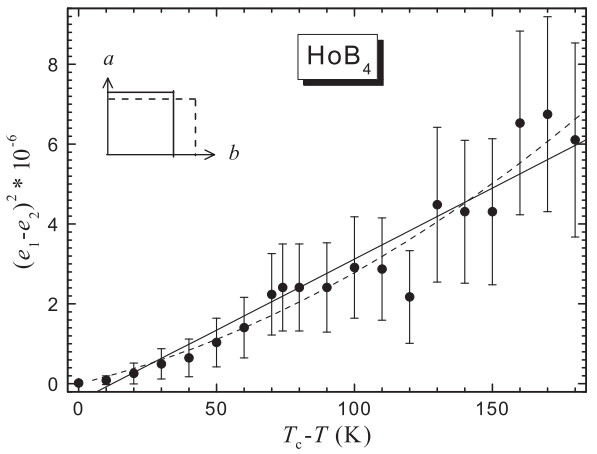

Fig. 9. Square of the symmetry breaking spontaneous strain, $(e_1–e_2)^2$, as a function of $(T_c–T)$. The inset graph indicates the unit cell distortion of the tetragonal-to-orthorhombic transition.

$\varepsilon_s = e_1 - e_2$. In terms of Landau thermodynamics, ε_s is proportional to the order parameter *Q* in the free-energy expansion for a ferroelastic transition. For a continuous phase transition one has $Q = A|T_c - T|^{0.5}$, and thus $\varepsilon_s^2 = (e_1 - e_2)^2 \sim (T_c - T)$. However, ε_s^2 is not exactly a linear function of $(T_c - T)$ in the present case (Fig. 9), suggesting that ε_s may not be the only driving mechanism of the observed phenomenon.

Unexpectedly, the orthorhombic distortion in HoB_4 upon decreasing temperature begins at about 285 K, *i.e.* well above the Néel temperature T_{N1}. Therefore, the physical mechanism of the distortion cannot be related to magnetic ordering. We suggest that the lattice behavior is connected with individual features of the HoB_4 sample, determined by inherent, built-in static strains due to geometric frustration in the Ho^{3+} sublattice and crystal mosaicity. The strains may produce spatial perturbations in the crystal field of the 4*f* electronic levels, causing local short-range quadrupolar ordering within microclusters of random distribution. Thus, there are competing unit cell

configurations with $a < b$ and $a > b$. The correlation lengths within and between the clusters increase with decreasing temperature, thereby forming elastic domains. This effect is visible in Fig. 8, where the scatter of the data reflects a cumulative, step-like strain evolution. Eventually, two dominating {1 1 0} domains aligned perpendicularly to the *c*-axis are formed in the equilibrium state.

In conclusion, our experiment shows that the paramagnetic phase I of HoB_4 below room temperature is not tetragonal all the way down to the Néel temperature T_{N1}, as is usually assumed. In fact, the microstructure consists of clusters of orthorhombic symmetry, and the hitherto assumed tetragonal unit cell corresponds to averaging over those clusters. The Laue photograph (Fig. 1) indicates a perfect monodomain structure, but high-resolution synchrotron radiation has allowed detecting these elastic domains. Notwithstanding, the single crystals are of high quality at the macroscopic level.

A crystallographic phase transition at a critical temperature T_c, which is higher than the Néel temperature T_N, has so far been reported only for the rare-earth tetraboride TbB_4 ($T_c = 80$ K and $T_N = 43$ K) [57]. That transition was considered driven either by strong electron–lattice coupling or by quadrupole–quadrupole interactions between Tb ions. We suggest here that the distortion developing in HoB_4 below room temperature is due to strong lattice–quadrupole couplings. Limitations of the present experimental temperature range did not allow probing the paramagnetic region all the way down to T_{N1} (Figs. 7–9). However, strain enhancement is likely to continue below 100 K. The resulting symmetry change will affect the magnetic interactions and therefore, at sufficiently large distortion, magnetic order will appear.

Fig. 10 shows the compression curve of HoB_4. A fit of the Birch–Murnaghan equation of state to the experimental pressure–volume data points gives a zero-pressure bulk modulus $B_0 = 195(5)$ GPa. This value compares well with the calculated values 198.2 GPa (LSDA + *U*) and 188.4 GPa (LSDA). Thus, the experimental value of the bulk modulus is in between the predictions of LSDA and LSDA + *U* calculations. This is also true for the unit cell volume (Table 2). To the best of our knowledge, there are no other experimental or theoretical values of the bulk modulus for HoB_4 published in the literature.

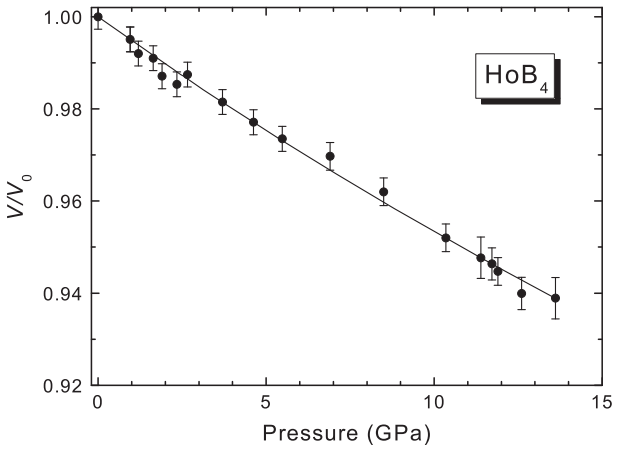

Fig. 10. Compression curve of HoB_4. The solid line is the fit of the Birch–Murnaghan Eq. (3) to the experimental pressure–volume data points.

The fact that the results of LSDA and LSDA + *U* calculations agree almost equally well with experiment is somewhat surprising, since the manifold of Ho *f*-electrons is highly correlated, and one would expect an improved description with the inclusion of the Coulomb correlation effects in the LSDA + *U* approach. However, bonding and hence the pressure–volume relation is primarily determined by the boron *p*-electrons, which are described similarly in the two approaches, apart from the difference in hybridization with Ho *f*-electrons. Other aspects of the electronic structure predicted by LSDA are less satisfactory. Thus, the spin magnetic moments differ by 0.55 μ_B in the two approaches ($M_s = 3.46\ \mu_B$ in LSDA and $M_s = 4.01\ \mu_B$ in LSDA + *U*). The LSDA + *U* value is in close agreement with the ideal value $M_s = 4.0\ \mu_B$ for a trivalent Ho (f^{10}) ion, which is what the LSDA + *U* approach is designed to accomplish, and which is also what the experimentally observed moment suggests [23]. In LSDA, on the other hand, the minority *f*-bands fall around the Fermi level and hybridize with the boron *p*-electrons, leading to a total occupation number of 4*f*-electrons that is higher than in LSDA + *U* by more than 0.5 electrons. Considering the above arguments, we are giving preference to our calculated bulk modulus 198.2 GPa, which corresponds to the LSDA + *U* approach.

5. Conclusions

The borides ScB_2, YB_4 and HoB_4 are hard materials with bulk modulus values in the range 180–190 GPa, while TiB_2 may be classified as a superhard material with a bulk modulus in the range 250–260 GPa. There is good agreement between experimental and theoretical values of the bulk modulus and other elastic constants for all substances. In this paper, we report the first experimental and theoretical values of the bulk modulus for HoB_4 (195(5) and 198.2 GPa, respectively), and the first experimental values of the bulk modulus for ScB_2 (196(2) GPa) and YB_4 (185(4) GPa). Values of the thermal expansion coefficient have been determined for ScB_2 and HoB_4 at 293, 200 and 100 K. No pressure-induced phase transformation has been observed for any of the above borides up to about 20 GPa. A continuous temperature-driven orthorhombic distortion is observed for HoB_4 below 285 K.

Acknowledgements

We wish to express our sincere thanks to Dr. Natalya Shitsevalova, who has been instrumental in writing this paper. We thank Hasylab/DESY for permission to use the synchrotron radiation facility, and Dr. Wolfgang Morgenroth for helpful assistance at Station D3. We are grateful to

Prof. Peter Herzig for communicating his results for YB_4 prior to publication. L.G. and J.S.O. gratefully acknowledge financial support from the Danish Natural Sciences Research Council through DANSCATT. K.R.B. acknowledges CMSD, University of Hyderabad, for use of computational facilities.

References

[1] Johnson RW, Daane AH. J Chem Phys 1963;38:425.
[2] Lönnberg B. J Less-Common Met 1988;141:145.
[3] Shveikin GP, Ivanovskii AL. Russian Chem Rev 1994;63:711.
[4] Munro RG. J Res Natl Inst Stand Technol (NIST) 2000;105:709.
[5] Nagamatsu J, Hakagawa N, Muranaka T, Zenitani Y, Akimitsu J. Nature 2001;410:63.
[6] Kortus J, Mazin II, Belashchenko KD, Antropov VP, Boyer LL. Phys Rev Lett 2001;86:4656.
[7] Belashchenko KD, van Schilfgaarde M, Antropov VP. Phys Rev B 2001;64:092503.
[8] Perottoni CA, Pereira AS, da Jornada JAH. J Phys: Condens Matter 2000;12:7205.
[9] Milman V, Warren MC. J Phys Condens Matter 2001;13:5585.
[10] Vajeeston P, Ravindran P, Ravi C, Asokamani R. Phys Rev B 2001;63:045115.
[11] Shein IR, Ivanovskii AL. J Phys: Condens Matter 2008;20:415218.
[12] Wang C-L, Yu B-H, Huo H-L, Chen D, Sun H-B. Chin Phys B 2009;18:1248.
[13] Zhang M, Wang H, Wang H, Zhang X, Iitaka T, Ma Y. Inorg Chem 2010;49:6859.
[14] Grechnev GE, Fedorchenko AV, Logosha AV, Panfilov AS, Svechkarev IV, Filippov VB, et al. J Alloys Compds 2009;481:75.
[15] Okamoto NL, Kusakari M, Tanaka K, Inui H, Otani S. Acta Mater 2010;58:76.
[16] Margadonna S, Muranaka T, Prassides K, Maurin I, Brigatti K, Iberson RM, et al. J Phys: Condens Matter 2001;13:L795.
[17] Etourneau J, Mercurio JP, Berrada A, Hagenmuller P. J Less-Common Met 1979;67:531.
[18] Fisk Z, Maple MB, Johnston DC, Wolf LD. Solid State Commun 1981;39:1189.
[19] Koehler WC, Mook HA, Fisk Z, Maple MB. J Appl Phys 1982;53:1966.
[20] Kosaka M, Onodera H, Ohoyama K, Ohashi M, Yamaguchi Y, Nakamura S, et al. Phys Rev B 1998;58:6339.
[21] Watanuki R, Sato G, Suzuki K, Ishihara M, Yanagisava T, Nemoto Y, et al. J Phys Soc Jpn 2005;74:2169.
[22] Okuyama D, Matsumura T, Nakao H, Murakami Y. J Phys Soc Jpn 2005;74:2434.
[23] Yin ZP, Pickett WE. Phys Rev B 2008;77:035135.
[24] Okuyama D, Matsumura T, Iwasa K, Murakami Y. J Magn Magn Mater 2007;310:e152.
[25] Okuyama D, Matsumura T, Mouri T, Ishikava N, Ohoyama K, Hiraka H. J Phys Soc Jpn 2008;77:044709.
[26] Kim JY, Cho BK, Han SH. J Appl Phys 2009;105:07E116.
[27] Olsen JS, Waskowska A, Gerward L, Vaitheeswaran G, Kanchana V, Svane A. High Press Res 2011;31:3.
[28] Levchenko G, Lyaschenko A, Baumer V, Evdokimova A, Filippov VB, Paderno Yu. J Solid State Chem 2006;179:2949.
[29] Pluzhnikov VB, Svechkarev IV, Dukhnenko AV, Levchenko AV, Filippov VB, Chopnik A. Low Temp Phys 2007;33:350.
[30] Evdokimova A, Nizhankovskii V, Pluzhnikov V, Shitsevalova N. In:16th International symposium on boron, borides and related materials (ISBB), Matsue, Japan; 2008. p. 159 [abstracts].
[31] Zogal OJ, Florian P, Massiot D, Paluch S, Shitsevalova N, Borshchevsky DF. Solid State Commun 2009;149:693.
[32] Massalski TV. Binary alloy phase diagrams. 2nd ed. Materials Park, OH: ASM International; 1996.
[33] Decker DL. J Appl Phys 1971;41:3239.
[34] Mao HK, Xu J, Bell PM. J Geophys Res 1986;91:4673.
[35] Werner P-E. Arkiv Kemi 1969;31:513.
[36] Birch FJ. Phys Rev 1947;71:809.
[37] Zalkin A, Templeton DH. Acta Cryst 1953;6:269.
[38] Segall MD, Lindan PLD, Probert MJ, Pickard CJ, Hasnip PJ, Clark SJ. J Phys: Condens Matter 2002;14:2717.
[39] Vanderbilt D. Phys Rev B 1990;41:7892.
[40] Perdew JP, Burke K, Ernzerhof M. Phys Rev Lett 1996;77:3865.
[41] Monkhorst HJ, Pack JD. Phys Rev B 1976;13:5188.
[42] Andersen OK. Phys Rev B 1975;12:3060.
[43] Methfessel M, van Schilfgaarde M, Casali RA. In: Dreysse H, editor. Lecture notes in physics, vol. 535. Berlin: Springer-Verlag; 2000. p. 114.
[44] Pethukov AG, Mazin II, Chionel L, Lichtenstein AI. Phys Rev B 2003;67:153106.
[45] Moehr S, Mueller-Bushbaum H, Grin Y, von Schnering HG. Zeit Anorg Allgem Chem 1996;622:1035.
[46] Peng F, Fu H-Z, Cheng X-L. Physica B 2007;400:83.
[47] Panda KB, Chandran KSR. Comput Mater Sci 2006;35:134.
[48] Pereira AS, Perottoni CA, da Jornada JAH, Léger JM, Haines J. J Phys: Condens Matter 2002;14:10615.
[49] Amulele GM, Manghnani MH, Somayazulu M. J Appl Phys 2006;99:023522.
[50] Spoor PS, Maynard JD, Pan MJ, Green DJ, Hellmann JR, Tanaka T. Appl Phys Lett 1997;70:1959.
[51] Dodd SP, Cankurtaran M, Saunders GA, James B. J Mater Sci 2001;36:3989–96.
[52] Guette A, Vlasse M, Etourneau J, Naslain R. C R Acad Sci (Paris) Ser C 1980;291:145.
[53] Jäger B, Paluch S, Wolf W, Herzig P, Zogal OJ, Shitsevalova N. J Alloys Compds 2004;383:232.
[54] Shastry B, Sutherland BS. Physica B + C 1981;108:1069.
[55] Severyanina EN, Dudnik EM, Paderno YB. Poroshkovaya Metallurgiya 1972;12:72.
[56] Salje E. Ferroelectrics 1990;104:111.
[57] Heiba Z, Schäfer W, Jansen E, Will G. J Phys Chem Solids 1986;47:651.